CHEMISTRY OF MATERIALS

Article

pubs.acs.org/cm

$LaMn_3Ni_2Mn_2O_{12}$: An A- and B-Site Ordered Quadruple Perovskite with A-Site Tuning Orthogonal Spin Ordering

Yun-Yu Yin,[†] Min Liu,[†] Jian-Hong Dai,[†] Xiao Wang,[†] Long Zhou,[†] Huibo Cao,[‡] Clarina dela Cruz,[‡] Chien-Te Chen,[§] Yuanji Xu,[†] Xi Shen,[†] Richeng Yu,[†] José Antonio Alonso,[∥] Angel Muñoz,[⊥] Yi-Feng Yang,*[,†,#] Changqing Jin,[†,#] Zhiwei Hu,[▽] and Youwen Long*[,†,#]

[†]Beijing National Laboratory for Condensed Matter Physics, Institute of Physics, Chinese Academy of Sciences, Beijing 100190, China

[‡]Quantum Condensed Matter Division, Neutron Scattering Science Directorate, Oak Ridge National Laboratory, Oak Ridge, Tennessee 37831, United States

[§]National Synchrotron Radiation Research Center, Hsinchu 30076, Taiwan, ROC

[∥]Instituto de Ciencia de Materiales de Madrid, CSIC, Cantoblanco, Madrid E-28049, Spain

[⊥]Universidad Carlos III, Avenida Universidad 30, E-28911 Leganés-Madrid, Spain

[#]Collaborative Innovation Center of Quantum Matter, Beijing 100190, China

[▽]Max Planck Institute for Chemical Physics of Solids, Dresden 01187, Germany

Supporting Information

ABSTRACT: A new oxide, $LaMn_3Ni_2Mn_2O_{12}$, was prepared by high-pressure and high-temperature synthesis methods. The compound crystallizes in an $AA'_3B_2B'_2O_{12}$-type A-site and B-site ordered quadruple perovskite structure. The charge combination is confirmed to be $LaMn^{3+}{}_3Ni^{2+}{}_2Mn^{4+}{}_2O_{12}$, where La and Mn^{3+} are 1:3 ordered at the A and A′ sites and the Ni^{2+} and Mn^{4+} are also distributed at the B and B′ sites in an orderly fashion in a rocksalt-type manner, respectively. A G-type antiferromagnetic ordering originating from the A′-site Mn^{3+} sublattice is found to occur at $T_N \approx 46$ K. Subsequently, the spin coupling between the B-site Ni^{2+} and B′-site Mn^{4+} sublattices leads to an orthogonally ordered spin alignment with a net ferromagnetic component near $T_C \approx 34$ K. First-principles calculations demonstrate that the A′-site Mn^{3+} spins play a crucial role in determining the spin structure of the B and B′ sites. This $LaMn_3Ni_2Mn_2O_{12}$ provides a rare example that shows orthogonal spin ordering in the B and B′ sites assisted by ordered A-site magnetic ions in perovskite systems.

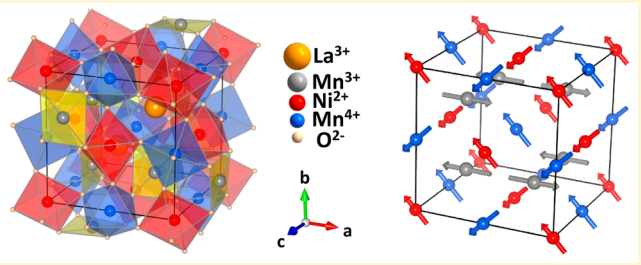

INTRODUCTION

A-Site ordered perovskites with a chemical formula of $AA'_3B_4O_{12}$ exhibit a wide variety of interesting physical properties such as intermetallic charge transfer, charge disproportionation, colossal magnetoresistance, a huge dielectric constant, negative thermal expansion, multiferroicity, etc.[1−14] Compared with a simple ABO_3 perovskite in which the A site is usually occupied by a larger alkali metal, alkaline earth, or rare earth, the A′ site in the ordered perovskite $AA'_3B_4O_{12}$, like the B site, can accommodate a transition metal (TM) ion with a smaller ionic radius. As a result, heavily tilted BO_6 octahedra and square-coordinated $A'O_4$ units occur as illustrated in Figure 1. The TM ions with strong Jahn−Teller (JT) distortions like Mn^{3+} and Cu^{2+} are thus favorable for occupation of the A′ site with square-planar coordination. The distinct electronic configurations between Mn^{3+} ($t_{2g}{}^3e_g{}^1$) and Cu^{2+} ($t_{2g}{}^6e_g{}^3$) ions can lead to essentially different magnetic and electrical transport properties in $AMn^{3+}{}_3B_4O_{12}$ and $ACu^{2+}{}_3B_4O_{12}$ families. In general, two independent long-range antiferromagnetic (AFM) phase transitions arising from the B-site TM ions and the A′-site Mn^{3+} ions take place in $AMn_3B_4O_{12}$,[15−17] whereas collinear ferromagnetic (FM) or ferrimagnetic Cu^{2+}−B interactions usually occur in $ACu_3B_4O_{12}$,[18] giving rise to a single magnetic transition. The long-range FM behavior has never been found in the family of $AMn^{3+}{}_3B_4O_{12}$.

In 3*d* TM oxides, the well-known Goodenough−Kanamori (GK) rules[19,20] can often give a feasible determination of the sign of spin superexchange interactions. For example, in the B-site ordered double perovskite A_2NiMnO_6 family (A = Sc, In, Y, Bi, or a rare earth) with Ni^{2+} ($t_{2g}{}^6e_g{}^2$) and Mn^{4+} ($t_{2g}{}^3e_g{}^0$) electronic configurations, the GK rules predict a FM interaction between the half-filled e_g orbitals of Ni^{2+} and the empty e_g orbitals of Mn^{4+} via a straight (or close to straight) Ni^{2+}−O−

Received: September 9, 2016
Revised: November 20, 2016
Published: November 22, 2016

DOI: 10.1021/acs.chemmater.6b03785
Chem. Mater. 2016, 28, 8988−8996

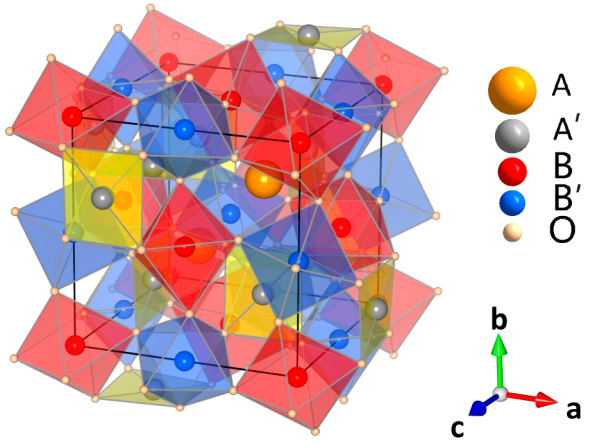

Figure 1. Crystal structure of both A- and B-site ordered $AA'_3B_2B'_2O_{12}$-type quadruple perovskite with $Pn\bar{3}$ symmetry. Atomic positions: A 2*a* (0.25, 0.25, 0.25), A′ 6*d* (0.25, 0.75, 0.75), B 4*b* (0, 0, 0), B′ 4*c* (0.5, 0.5, 0.5), and O 24*h* (*x*, *y*, *z*).

Mn^{4+} pathway, while an AFM interaction is expected to occur if the Ni^{2+}−O−Mn^{4+} bonding becomes close to 90°. On the basis of this criterion, a multiferroic compound Bi_2NiMnO_6 with coexisting FM and ferroelectric properties was successfully obtained.[21] Figure 2 shows the magnetic phase diagram of the

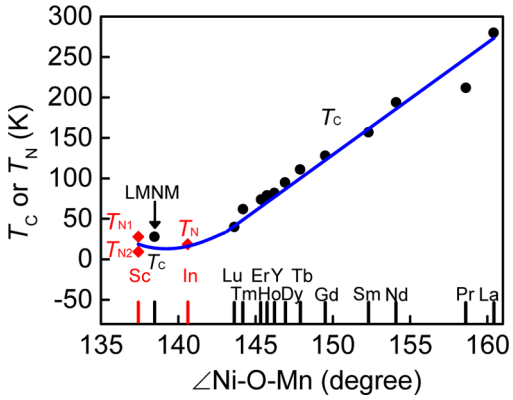

Figure 2. Magnetic ordering temperature as a function of the average Ni−O−Mn bond angle in the A_2NiMnO_6 family and LMNM. T_N is the AFM Néel temperature (red diamonds), and T_C is the FM Curie temperature (black circles). The blue line is a guide for the eyes.

A_2NiMnO_6 family. For a smaller A-site ion like Sc^{3+} or In^{3+}, the related compounds show AFM orderings.[22,23] With increasing A-site ionic size, the magnetism changes from canted FM ordering (A = Lu^{3+}, Tm^{3+}, Er^{3+}, Ho^{3+}, Y^{3+}, or Tb^{3+})[24−28] to collinear FM alignments (A = Nd^{3+} or La^{3+}),[29,30] accompanied by a monotonous rising of the FM Curie temperature (T_C). This systematic variation suggests that if Ni^{2+} and Mn^{4+} ions can be introduced in an ordered fashion into the B site in $AMn_3B_4O_{12}$ in a rocksalt-type manner, as the A_2NiMnO_6 family does, long-range FM behavior can be realized for a larger A-site cation like La^{3+}.

In this paper, a new $AA'_3B_2B'_2O_{12}$-type A-site and B-site ordered perovskite oxide, $LaMn_3Ni_2Mn_2O_{12}$ (LMNM), was designed and prepared for the first time under high-pressure and high-temperature conditions. Our measurements show that the A′-site Mn^{3+} spins are ordered into a collinear G-type AFM structure at $T_N \approx 46$ K. On the other hand, the B-site Ni^{2+} and B′-site Mn^{4+} ions are ordered into a 90° canted spin alignment at $T_C \approx 34$ K, leading to a net FM moment of ∼6.6 μ_B fu^{-1} at 2 K. This is the first observation of orthogonal spin ordering in all of the A-site (and B-site) ordered quadruple perovskite systems discovered so far. Theoretical calculations reveal that the competing exchange interactions among the three different magnetic ions (A′-site Mn^{3+}, B-site Ni^{2+}, and B′-site Mn^{4+}) are mainly responsible for this unique spin feature.

EXPERIMENTAL AND CALCULATION SECTION

Polycrystalline sample LMNM was prepared from highly pure (>99.9%) La_2O_3, Mn_2O_3, MnO_2, and NiO starting materials with a 1:3:4:4 mole ratio. The finely mixed starting materials were charged into a gold capsule and treated at 8 GPa and 1400 K for 60 min in a cubic anvil-type high-pressure apparatus. Then the reaction was quenched to room temperature (RT) before the pressure was slowly released. X-ray powder diffraction (XRD) was performed on a Rigaku diffractometer equipped with Cu Kα radiation. The obtained XRD data were analyzed by the Rietveld method[31] with the GSAS program.[32] High-resolution selected area electron diffraction (SAED) was performed at RT along the [1−10] zone axis by a Philips-CM200 field emission transmission electron microscope. The valence states of Mn and Ni ions at RT were determined by soft X-ray absorption spectroscopy (XAS) at the Mn-$L_{2,3}$ and Ni-$L_{2,3}$ edges measured at the Dragon beamline of the Taiwan National Synchrotron Research Center. Temperature-dependent neutron powder diffraction (NPD) was measured at HB-2A at the High Flux Isotope Reactor (HFIR) of Oak Ridge National Laboratory (ORNL) with a wavelength λ of 2.41 Å. The diffraction data were collected at 300, 200, 40, and 3 K. The FullProf program[33] was used to refine the NPD data on the basis of the Rietveld method. The magnetic susceptibility and magnetization were measured in a superconducting quantum interference device magnetometer (Quantum Design, MPMS-VSM). Both zero-field cooling (ZFC) and field cooling (FC) modes were used to measure the magnetic susceptibility between 2 and 300 K at 0.01 and 1 T. Magnetization was measured at fields ranging from −7 to 7 T at selected temperatures of 100, 60, 40, and 2 K. Specific heat (C_p) data were collected by a pulse relaxation method on a physical property measurement system calorimeter (Quantum Design, PPMS-9T). Different magnetic fields (0 and 1 T) were applied for this measurement upon cooling from 75 to 2 K.

The electronic structures were analyzed by density functional theory (DFT) calculations using the full-potential linearized augmented plane-wave (LAPW) method,[34] with the augmented plane-wave plus local orbital implementation[35] in both the WIEN2K code[36] and the noncollinear WIENNCM code.[37] To include the strong correlations in the transition metal elements, we took the generalized gradient approximation Perdew, Burke, and Ernzerhof (GGA-PBE) exchange correlation potential[38] with effective Coulomb repulsions (U^{eff}) of 3.0 eV for Mn and 5.0 eV for Ni in the GGA + *U* calculations with a method of self-interaction correction introduced by Anisimov.[39] The muffin tin radii are 2.50 au for La, 1.90 au for Mn, 2.00 au for Ni, and 1.60 au for O. The maximal modulus for the reciprocal vectors (K_{max}) was chosen such that RMT × K_{max} = 8.0. The lattice parameters and ionic positions derived from the NPD refinement at 3 K were used in the calculations without performing any structural or ionic relaxations. The Brillouin zone samplings were checked by directly increasing the density of the *k*-point meshes until convergence was reached, that is, until the changes in calculated properties were insignificant. Finally, 1000 *k*-point meshes in the Brillouin zone were used.

RESULTS AND DISCUSSION

The high-pressure product LMNM we made was found to be insulating with a resistivity (ρ) of >10^5 Ω cm^{-1} at RT. The sample quality and crystal structure were characterized by XRD, SAED, and NPD. Figure 3a shows the XRD pattern measured at RT. Because of the similar scattering factors of Ni and Mn, the X-ray is not sufficiently sensitive to distinguish the ordered

DOI: 10.1021/acs.chemmater.6b03785
Chem. Mater. 2016, 28, 8988−8996

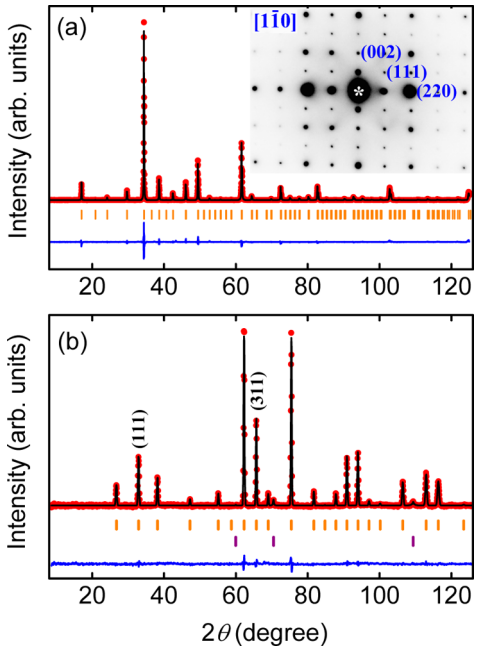

Figure 3. Rietveld refinements for (a) the XRD pattern recorded at RT and (b) the NPD pattern recorded at 300 K for LMNM. The observed (red circles), calculated (black line), and difference (blue line) values are shown. Allowed Bragg reflections are indicated by ticks (top). The lower ticks shown in panel b present the small amount of impurity phase NiO (<1.2 wt %). The inset in panel a shows an SAED pattern along the [1−10] zone axis taken at RT.

distribution for these two atoms. The SAED was thus measured as presented in the inset of Figure 3a. One can find bright diffraction spots with $h + k + l$ = odd such as the (111) spot, providing convincing evidence of the B-site ordered distribution between Ni and Mn in a rocksalt-type manner. The Rietveld analysis for the XRD pattern further reveals that LMNM crystallizes in both A- and B-site ordered $AA'_3B_2B'_2O_{12}$-type quadruple perovskite structures in space group $Pn\bar{3}$ (No. 201). As shown in Figure 1, in this crystal symmetry, the A-site La and A′-site Mn occupy the fixed 2*a* (0.25, 0.25, 0.25) and 6*d* (0.25, 0.75, 0.75) sites while the B-site Ni and B′-site Mn occupy the fixed 4*b* (0, 0, 0) and 4*c* (0.5, 0.5, 0.5) sites, respectively. Furthermore, this specially ordered perovskite structure can be confirmed by NPD as shown in Figure 3b, where the characteristic peaks reflecting the rocksalt-type B-site ordering like (111) and (311) peaks present sharply. The high-pressure product LMNM thus possesses the same crystal structure found in $CaCu_3Ga_2Sb_2O_{12}$[40] and $CaCu_3Fe_2Re_2O_{12}$.[41] The structural refinements based on the NPD data obtained at 300 K show a nearly ideal 1:3 ordering between the A-site La and A′-site Mn ions (i.e., these two sites are almost fully occupied by La and Mn, respectively), and the 4*c* B′ site is also nearly completely occupied by Mn. As far as the 4*b* B site is considered, a small amount of Mn (∼11%) is found to substitute for the Ni site. In addition, the occupancy factor of oxygen is very close to unity, suggesting that our LMNM is chemically stoichiometric. The refined structural parameters are listed in Tables 1 and 2. On the basis of the related bond lengths, the bond valence sum (BVS)[42,43] calculations indicate the charge combination to be $LaMn^{3+}{}_3Ni^{2+}{}_2Mn^{4+}{}_2O_{12}$ [+2.98 for the A′-site Mn, +2.15 for the B-site Ni, and +3.97 for the B′-site Mn at 300 K (see Table 2)], in agreement with the XAS measurements shown below. It means that the strong JT-distorted Mn^{3+} ions occupy the square-coordinated $A'O_4$ units, while the tilted but rigid BO_6

Table 1. Structural Parameters Obtained from the Rietveld Refinements of NPD (3, 40, 200, 300 K) and XRD (RT) Data for LMNM[a]

T (K)	3	40	200	300	RT
space group	$Pn\bar{3}$	$Pn\bar{3}$	$Pn\bar{3}$	$Pn\bar{3}$	$Pn\bar{3}$
a (Å)	7.35692(20)	7.35860(9)	7.36198(12)	7.36863(8)	7.37478(3)
O_x	0.2590(3)	0.2583(2)	0.2583(2)	0.2592(2)	0.254(10)
O_y	0.4288(4)	0.4271(3)	0.4269(2)	0.4275(3)	0.4340(5)
O_z	0.5596(4)	0.5607(2)	0.5608(2)	0.5608(2)	0.5673(5)
G (Ni_{4b})	0.890	0.890	0.890(4)	0.912(6)	0.96(13)
G (Mn_{4b})	0.110	0.110	0.110(4)	0.088(6)	0.08(11)
G (Ni_{4c})	0.014	0.014	0.014(4)	0.001(1)	0.03(11)
G (Mn_{4c})	0.986	0.986	0.986(4)	0.999(1)	0.91(13)
G (O)	1.0	1.0	1.0	1.04(2)	1.043(10)
M (Mn_{6d}) (μ_B)	2.94(5)	1.60(4)	–	–	–
M (Ni_{4b}) (μ_B)	0.65(3)	–	–	–	–
M (Mn_{4c}) (μ_B)	0.44(3)	–	–	–	–
B_{iso} (La) (Å^2)	0.200	0.12(12)	0.30(11)	1.00(15)	0.014(6)
B_{iso} (Mn_{6d}) (Å^2)	0.200	1.5(1)	1.58(12)	1.80(17)	0.016(3)
B_{iso} (Ni_{4b}) (Å^2)	0.400	0.42(6)	0.38(7)	0.62(13)	0.017(7)
B_{iso} (Mn_{4c}) (Å^2)	0.200	0.2	0.2	0.2	0.009(3)
B_{iso} (O) (Å^2)	0.250	0.37(8)	0.43(10)	0.46(17)	0.014(5)
χ^2	6.26	2.39	1.64	4.51	3.49
R_{wp} (%)	7.98	6.13	5.03	6.88	12.49
R_p (%)	6.35	4.83	3.84	5.44	10.24

[a]Space group $Pn\bar{3}$ (No. 201), origin choice 2, where the atomic positions are La 2*a* (0.25, 0.25, 0.25), Mn 6*d* (0.25, 0.75, 0.75), Ni 4*b* (0, 0, 0), Mn 4*c* (0.5, 0.5, 0.5), and O 24*h* (*x*, *y*, *z*). *G* represents the site occupation factor; *M* represents the ionic spin moment. The site occupancy for O was refined for the 300 K NPD pattern, resulting in a stoichiometric value within 2 times the standard deviation. For the lower temperatures, it was fixed to unity.

DOI: 10.1021/acs.chemmater.6b03785
Chem. Mater. 2016, 28, 8988−8996

Table 2. Selected Bond Lengths and Angles and BVS Calculations for LMNM Obtained from Rietveld Refinements of NPD Data[a]

T (K)	3	40	200	300
Mn_{6d}–O (Å) (×4)	1.909(1)	1.908(5)	1.908(4)	1.912(9)
(×4)	2.751(4)	2.755(1)	2.756(5)	2.756(1)
(×4)	3.296(3)	3.304(9)	3.306(2)	3.303(6)
Ni_{4b}–O (Å) (×6)	2.028(3)	2.025(2)	2.026(7)	2.033(9)
Mn_{4c}–O (Å) (×6)	1.905(5)	1.910(3)	1.911(4)	1.905(7)
Mn_{6d}–O–Mn_{6d} (deg)	102.7(4)	102.6(7)	102.6(8)	102.7(1)
Mn_{6d}–O–Ni_{4b} (deg)	107.9(7)	108.1(6)	108.1(8)	107.8(5)
Mn_{6d}–O–Mn_{4c} (deg)	113.2(6)	113.1(1)	113.1(5)	113.3(5)
Ni_{4b}–O–Mn_{4c} (deg)	138.4(6)	138.4(1)	138.3(6)	138.4(9)
BVS (Mn_{6d})	+3.009(3)	+3.010(9)	+3.010(3)	+2.978(7)
BVS (Ni_{4b})	+2.181(8)	+2.200(1)	+2.191(2)	+2.149(1)
BVS (Mn_{4c})	+3.974(4)	+3.922(1)	+3.910(5)	+3.971(2)

[a]The BVS values (V_i) were calculated using the formula $V_i = \sum_j S_{ij}$, and $S_{ij} = \exp[(r_0 - r_{ij})/0.37]$. In LMNM, r_0 = 1.760 Å for Mn_{6d}, r_0 = 1.753 Å for Mn_{4c}, and r_0 = 1.654 Å for Ni_{4b}. For Mn_{6d}, 12-coordinated oxygen atoms were used. For Ni_{4b} and Mn_{4c}, 6-coordinated oxygen atoms were used.

and $B'O_6$ octahedra accommodate the non-JT-distorted ions Ni^{2+} ($t_{2g}^6 e_g^2$) and Mn^{4+} ($t_{2g}^3 e_g^0$), respectively.

XAS is sensitive to the valence state and local environment of 3*d* TM ions. To further check the oxidation states of Mn and Ni ions in LMNM, soft XAS was measured. As shown in Figure 4a, the Ni-$L_{2,3}$ spectrum of LMNM lies at the same energy as that of the divalent reference $PbNi^{2+}O_3$[44] but is shifted by more than 1 eV to an energy lower than that of the trivalent reference $Nd_2Li_{0.5}Ni^{3+}{}_{0.5}O_4$,[45,46] confirming the Ni^{2+} valence state in LMNM. Furthermore, the multiplet spectral structure of LMNM is very similar to that of $PbNiO_3$, demonstrating the similar NiO_6 octahedral coordination in these two compounds. Figure 4b shows the Mn-$L_{2,3}$ XAS spectra of LMNM together with the A-site ordered perovskite $YMn^{3+}{}_3Al_4O_{12}$ (YMA)[47] as a Mn^{3+} reference with MnO_4 square local coordination and $SrMnO_3$ as a Mn^{4+} reference with MnO_6 octahedral local coordination.[48] One can see a gradual higher-energy shift from YMA to LMNM and further to $SrMnO_3$, indicating an increase in the Mn valence state. The dotted line in Figure 4b shows a simple superposition of YMA and $SrMnO_3$ with a 3:2 ratio. One can see that the superposition agrees well with the XAS spectrum of LMNM. Thus, the XAS features of LMNM are in accordance with the $LaMn^{3+}{}_3Ni^{2+}{}_2Mn^{4+}{}_2O_{12}$ charge configuration, as suggested by the BVS calculations. To the best of our knowledge, the LMNM presented here is the first A- and B-site ordered cubic quadruple perovskite with Mn^{3+} at the A′ site. In other reported isostructural compounds, the A′ site is always occupied by Cu^{2+}, for example, $CaCu_3Cr_2Sb_2O_{12}$,[49] $CaCu_3Fe_2Re_2O_{12}$,[41] $CaCu_3Fe_2Os_2O_{12}$,[50] etc. Although the A- and B-site orderings can form at lower temperatures in $NaMn_7O_{12}$ ($NaMn^{3+}{}_3Mn^{4+}{}_2Mn^{3+}{}_2O_{12}$) and $CaMn_7O_{12}$ ($CaMn^{3+}{}_3Mn^{4+}Mn^{3+}{}_3O_{12}$), the crystal structure is changed from cubic to monoclinic and rhombohedral, respectively.[12,15]

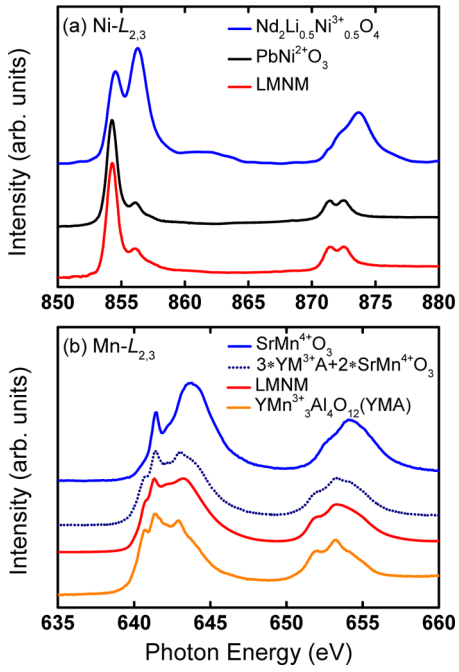

Figure 4. Normalized XAS of (a) Ni-$L_{2,3}$ edges of LMNM (red) and the references $PbNi^{2+}O_3$ (black) and $Nd_2Li_{0.5}Ni^{3+}{}_{0.5}O_4$ (blue) and (b) Mn-$L_{2,3}$ edges of LMNM (red) and the references $YMn^{3+}{}_3Al_4O_{12}$ (orange) and $SrMn^{4+}O_3$ (blue). The dotted line shows a simple superposition of $YMn_3Al_4O_{12}$ and $SrMnO_3$ with a 3:2 ratio.

Because three different atomic sites (A′, B, and B′) are accommodated by magnetic TM ions, it is interesting to study the spin interactions occurring among them. Figure 5a shows the temperature dependence of magnetic susceptibility measured at different fields. At first glance, the susceptibility just experiences a single FM-like sharp increase at low temperatures. At a small applied field of 0.01 T, the ZFC and FC susceptibility curves are separated from each other below the transition temperature. However, if a larger field (e.g., 1 T) is applied to overcome the domain wall energy, these two curves become coincident. In addition, when we examine the second derivative of the inverse susceptibility measured at 0.01 T as a function of temperature, one can find two clear anomalies (inset of Figure 5a), implying double magnetic phase transitions. To further confirm these two possible spin transitions, the specific heat was measured at zero field and 1 T. As shown in Figure 5b, two sharp λ-type anomalies are also observed in specific heat near $T_N \approx 46$ K and $T_C \approx 34$ K at zero field. When a magnetic field is applied, T_N is nearly unchanged whereas T_C significantly increases. On the basis of these features, we conclude that LMNM experiences a long-range AFM transition around 46 K and then another FM-like transition at ∼34 K.

The magnetization data provide additional evidence of these two successive spin transitions. As shown in Figure 5c, the linear magnetization behavior above T_N is indicative of the paramagnetism. Between T_N and T_C, there is no canonical magnetic hysteresis, while some short-range FM coupling is observed as characterized by the magnetization curve measured at 40 K. Below T_C, however, the magnetic hysteresis loop is observed, confirming the long-range FM-like feature. At the lowest temperature we measured (2 K), the spin moment is not

DOI: 10.1021/acs.chemmater.6b03785
Chem. Mater. 2016, 28, 8988−8996

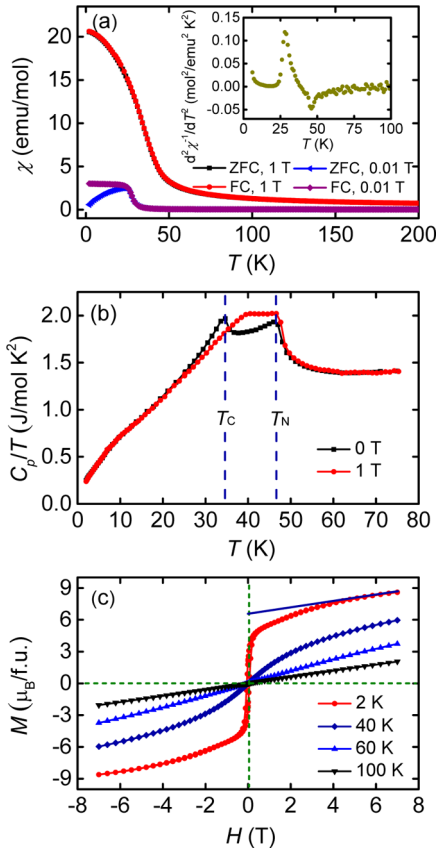

Figure 5. (a) Temperature dependence of magnetic susceptibility measured at 0.01 and 1 T. The inset shows the second derivative of the inverse susceptibility at 0.01 T. (b) Temperature dependence of specific heat measured at zero field and 1 T. (c) Magnetization measured at various temperatures.

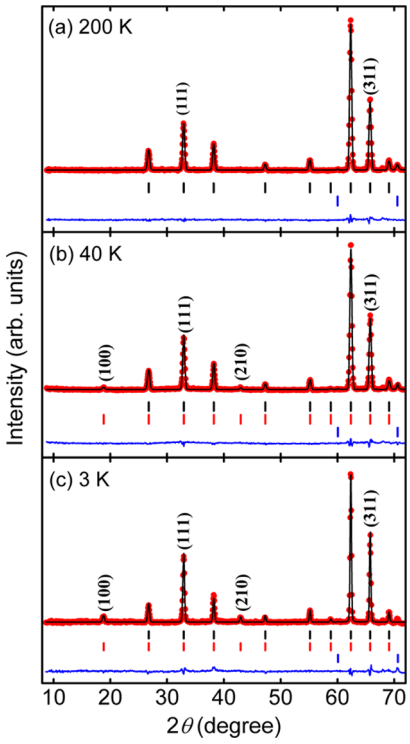

Figure 6. Rietveld refinements for the NPD patterns of LMNM collected at (a) 200, (b) 40, and (c) 3 K. The observed (red circles), calculated (black line), and difference (blue line) values are shown. The black, red, and blue ticks correspond to the allowed nuclear Bragg peaks, magnetic Bragg reflections, and the impurity phase NiO (<1.2 wt %), respectively.

completely saturated as the field increases to 7 T, suggesting the coexisting FM and AFM interactions at lower temperatures. When the AFM contribution is subtracted by a linear extrapolation (see the solid line in Figure 5c), the saturated FM moment is estimated to be 6.6 μ_B fu^{-1}. As mentioned above, in the A-site ordered $AMn_3B_4O_{12}$ family, the A′-site Mn^{3+} ions often induce an independent AFM ordering. The AFM transition occurring in LMNM thus most probably originates from the spin ordering of the A′-site Mn^{3+} sublattice. On the other hand, the adjacent Ni^{2+} ions with e_g^2 electrons and the Mn^{4+} ions with empty e_g orbitals can generate FM interactions,[21,30] so the FM-like phase transition of LMNM should be related to the spin interactions of the B/B′-site Ni^{2+}/Mn^{4+} sublattices. A collinear FM coupling between Ni^{2+} and Mn^{4+} will produce a 10.0 μ_B fu^{-1} saturation moment in a local electronic model in the insulating LMNM. The reduced moment observed in the experiment may suggest a noncollinear FM alignment, as will be revealed by NPD. In addition, the ZFC and FC susceptibility curves measured at 0.01 T separate from each other just below T_C not below T_N, also agreeing with a noncollinear FM structure as well as a collinear AFM one.

Temperature-dependent NPD was performed to clarify the specific spin structures. A detailed magnetic group theory analysis of the NPD data of LMNM is described in the Supporting Information. As shown in Figure 6a, the NPD pattern obtained at 200 K is essentially similar to that measured at 300 K. However, new neutron diffraction peaks like the (100) peak arising from the special spin ordering are observed at 40 K (below T_N). The magnetic ordering between T_N and T_C has thus been investigated from the NPD pattern obtained at this temperature on the basis of the Rietveld method. After the different solutions listed in Table S1 are checked, the best one is obtained if only the Mn magnetic atoms at the 6*d* site are ordered with the basis vectors given by Γ^8, where the coupling among the magnetic moments is $m_{1x} = m_{2x} = m_{3x} = -m_{4x} = -m_{5x} = -m_{6x}$. It means that the Mn atoms linked by the inversion center have their magnetic moments antiferromagnetically coupled. This solution is quite consistent with the magnetic and specific heat measurements. The results of the fitting are listed in Table S3. The good agreement between the experimental and calculated NPD data is presented in Figure 6b. Therefore, at 40 K, the magnetic structure determined from the NPD pattern corresponds to a collinear G-type AFM structure, in which each Mn^{3+} spin is antiferromagnetically coupled with the surrounding neighbors (Figure 7a). Note that some other $AMn_3B_4O_{12}$ perovskites such as $LaMn_3Cr_4O_{12}$[14] and $YMn_3Al_4O_{12}$[51] also have similar G-type AFM structure for the A′-site Mn^{3+} ions. If we assume that, at 40 K, the Ni atoms of the 4*b* site and the Mn atoms of the 4*c* site in LMNM also contribute to the magnetic ordering, it is not possible to correctly fit the experimental data. Therefore, we conclude that at T_N, first only the Mn^{3+} ions at the site 6*d* are ordered, and the rest of the magnetic ions become ordered at a lower temperature.

According to the magnetic susceptibility and specific heat measurements, another magnetic phase transition is observed at $T_C \approx 34$ K, although no essential change is observed in the

DOI: 10.1021/acs.chemmater.6b03785
Chem. Mater. 2016, 28, 8988−8996

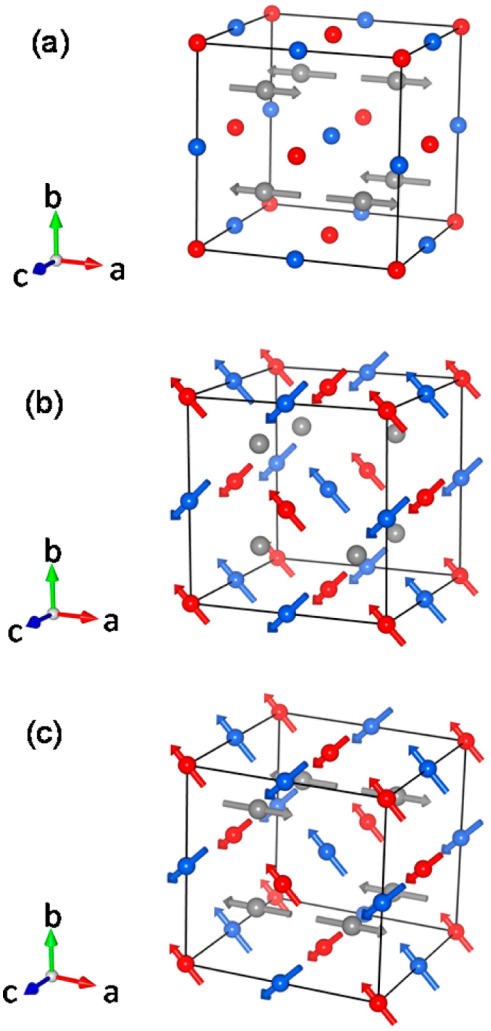

Figure 7. Schematic view of (a) the G-type AFM structure of the A′-site Mn^{3+} (gray), (b) the orthogonally ordered spin structure composed of the B-site Ni^{2+} (red) and the B′-site Mn^{4+} (blue), and (c) the total spin structure composed of the A′-, B-, and B′-site magnetic ions. For the sake of clarity, O and La have been omitted from the structures.

magnetic Bragg reflections of the NPD pattern collected at 3 K compared with that at 40 K, except an increase in the intensity (Figure 6c). As shown in Figure S1, when we examine the normalized NPD intensity as a function of temperature for magnetic peaks (100) and (111), the diffraction intensity for these two peaks sharply increases around T_N, and then divergence occurs below T_C. These features may also suggest two magnetic phase transitions. When the NPD pattern collected at 3 K is fitted, the best agreement is obtained if it is assumed that the 6*d* sublattice (i.e., A′-site Mn^{3+}) remains ordered with the same magnetic structure as that determined at 40 K and the 4*b* (B-site Ni^{2+}) and 4*c* (B′-site Mn^{4+}) sublattices are ordered according to the basis vectors of Ψ_{27} in Γ^7. The coupling among the magnetic moments for sites 4*b* and 4*c* shows a net FM component originating from the orthogonal spin ordering in the B and B′ sites (Figure 7b), in good agreement with the magnetization measurements.

Therefore, the total spin structure of LMNM below T_C contains the G-type arrangement concerning the A′-site Mn^{3+} cations, with the additional ordering of the B/B′-site Ni^{2+}/Mn^{4+} sublattices exhibiting an "umbrella"-like perpendicular magnetic structure, in such a way that there is a resulting FM component along the *a* axis (Figure 7c). The LMNM presented here thus provides the first example with orthogonal spin ordering in all of the A-site (and B-site) ordered perovskite systems yet discovered. In this spin structure model, the net local spin moment caused by the 90° canted Ni^{2+} and Mn^{4+} spins is theoretically 7.07 μ_B fu^{-1}, which is close to the experimental value (6.6 μ_B fu^{-1}) extrapolated from the magnetization measurement at 2 K. Note that there are two more exactly equivalent solutions with the net spin moments along the *b* and *c* axes, respectively.

The neutron refinements (see Table S3) at 3 K give spin moments of 2.94(8) μ_B for the A′-site Mn^{3+} ($S = 2$), 0.65(3) μ_B for the B-site Ni^{2+} ($S = 1$), and 0.44(3) μ_B for the B′-site Mn^{4+} ($S = {}^3/_2$). These values, especially the B- and B′-site moments, are considerably smaller than the spin-only expected ones. This may be attributed to the small amount of B- and B′-site disorder as well as the strong spin frustrations, as discussed below. In addition, the FM-like ordering caused by the Ni^{2+}−O−Mn^{4+} pathway in LMNM is found to deviate from the magnetic evolution criterion exhibited by members of the A_2NiMnO_6 family. As shown in Figure 2, the Ni^{2+}−O−Mn^{4+} bond angle in LMNM is 138.5°, which is located in the AFM region in the A_2NiMnO_6 series. This extraordinary deviation may suggest that the A′-site magnetic ions play some roles for the B- and B′-site magnetic interactions in LMNM.

To improve our understanding of the specific spin interactions among the three different transition metals in LMNM, first-principles theoretical calculations were performed on the basis of the structural parameters determined from NPD data at 3 K. For the sake of simplicity, we used the collinear magnetic configurations to calculate the specific spin interactions as described in detail in the Supporting Information. Actually, similar calculations were also adopted for Sr_2CoOsO_6,[52] which possesses a noncollinear spin structure, too. As shown in Figure 8a, eight potentially important spin exchange pathways are considered. For the A′-site Mn^{3+} spin sublattice, the nearest neighboring (NN) J_1^{eff} and the third-nearest neighboring (TNN) J_3^{eff} interactions overwhelm the small next-nearest neighboring (NNN) J_2^{eff} interaction and favor AFM ordering. In contrast, in the B- and B′-site octahedra, the NN B(Ni^{2+})−B′(Mn^{4+}) J_4^{eff}, NNN B(Ni^{2+})−B(Ni^{2+}) J_5^{eff}, and B′(Mn^{4+})−B′(Mn^{4+}) J_6^{eff} interactions are all FM coupling. These results are consistent with the magnetic measurements and NPD refinements. However, different from the reported $LaMn_3Cr_4O_{12}$, where A′−B intersite spin coupling is negligible, significant A′(Mn^{3+})−B(Ni^{2+}) J_7^{eff} and A′(Mn^{3+})−B′(Mn^{4+}) J_8^{eff} exchange interactions are presented in our LMNM. Moreover, the interaction energies of J_7^{eff} and J_8^{eff} are comparable to those of NN or NNN J_1^{eff} and J_4^{eff}–J_6^{eff}, strongly suggesting that the A′-site magnetic ions play an important role in the spin ordering of the B- and B′-site magnetic ions in LMNM. As shown in Figure 8b, the calculated density of states (DOS) demonstrates a wide energy gap of ∼1.5 eV, indicating the insulating behavior of LMNM as expected from the high-spin Ni^{2+} and Mn^{4+} states at the corner-sharing $B/B'O_6$ octahedra. In addition, the DOS values of the A′-site Mn^{3+}, B-site Ni^{2+}, and B′-site Mn^{4+} considerably overlap. It helps to explain the strong spin interactions among these magnetic ions. By comparison, in $LaMn_3Cr_4O_{12}$, the overlap of DOS values between the A′- and B-site ions is negligible.[53] Note that the comparable spin interactions J_4^{eff} (FM), J_7^{eff} (AFM), and

DOI: 10.1021/acs.chemmater.6b03785
Chem. Mater. 2016, 28, 8988−8996

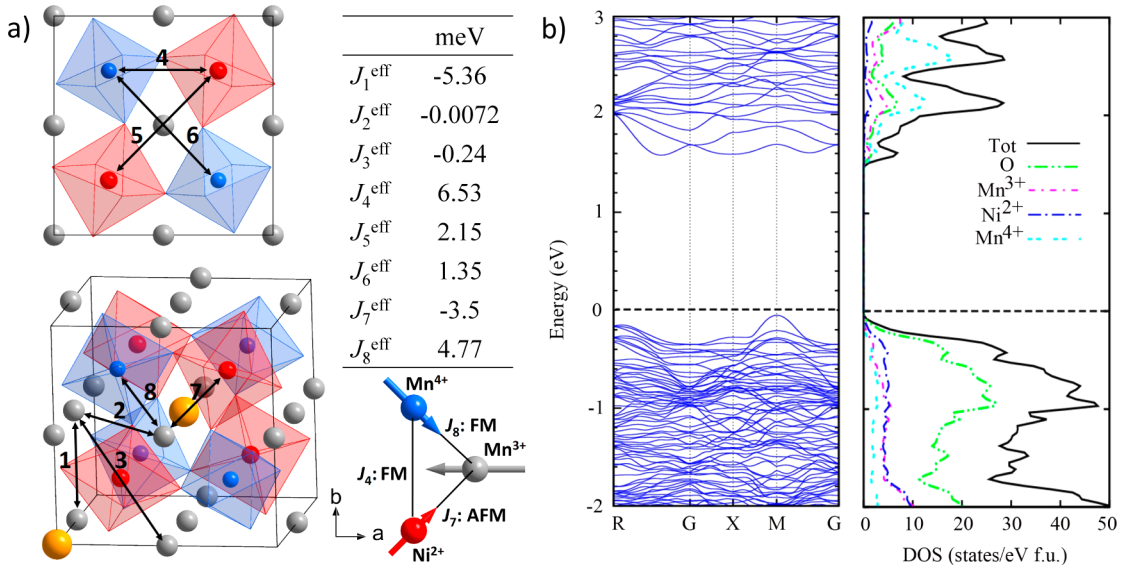

Figure 8. (a) Schematic view of the magnetic exchange pathways and magnetic frustration model among the A′-site Mn^{3+} (gray), B-site Ni^{2+} (red), and B′-site Mn^{4+} (blue) ions with the exchange constants determined from the theoretical calculations. (b) Total and atom-resolved DOS from calculations.

J_8^{eff} (FM) occurring among Mn^{3+}, Ni^{2+}, and Mn^{4+} spins can form strong magnetic geometrical frustrations (Figure 8a). These frustrations as well as the B- and B′-site disorder mentioned above are very plausibly the origin of the small ordered magnetic moments observed by neutrons, because the magnetic ordering cannot be fully developed. This is a well-known effect in many oxides, typically pyrochlores, where the existence of competing interactions given by the space group geometry prevents the establishment of a long-range magnetic ordering.[54]

CONCLUSIONS

In summary, we have prepared a new oxide, $LaMn_3Ni_2Mn_2O_{12}$, by high-pressure and high-temperature synthesis techniques. The compound is confirmed to be an A-site and B-site ordered cubic quadruple perovskite with $Pn\bar{3}$ symmetry with a $LaMn^{3+}{}_3Ni^{2+}{}_2Mn^{4+}{}_2O_{12}$ charge combination. It means that three magnetic ions occupy three different atomic positions, giving rise to interesting spin interactions. With the temperature decreasing to $T_N \approx 46$ K, an AFM phase transition is observed due to the collinear G-type AFM ordering of the A′-site Mn^{3+} spins. When the sample is further cooled to $T_C \approx 34$ K, a long-range FM-like phase transition takes place. NPD analysis reveals that the orthogonally ordered spin coupling between B-site Ni^{2+} and B′-site Mn^{4+} sublattices is responsible for this transition with a considerable net FM moment. The magnetic ground state is thus frustrated because of the coexisting FM and AFM interactions. Although most $AMn^{3+}{}_3B_4O_{12}$ perovskite compounds do not show significant A′−B intersite spin interactions, in the LMNM presented here, theoretical calculations demonstrate that both A′−B and A′−B′ pathways show considerable superexchange interactions comparable to those of A′−A′, B−B, and B′−B′ pathways. Therefore, the A′-site Mn^{3+} spins play an important role in determining the peculiar spin alignment for the B/B′-site Ni^{2+}/Mn^{4+} ions. The unique orthogonal spin ordering is thus realized in LMNM. This is its first observation in A-site (and B-site) ordered quadruple perovskites, opening a new way to design other special magnetic structures in ordered perovskite systems.

ASSOCIATED CONTENT

Supporting Information

The Supporting Information is available free of charge on the ACS Publications website at DOI: 10.1021/acs.chemmater.6b03785.

Detailed NPD refinements, magnetic structure representations, and DFT calculations (PDF)

AUTHOR INFORMATION

Corresponding Authors

*E-mail: yifeng@iphy.ac.cn.

*E-mail: ywlong@iphy.ac.cn.

ORCID

Youwen Long: 0000-0002-8587-7818

Notes

The authors declare no competing financial interest.

ACKNOWLEDGMENTS

The authors thank G. B. Li for his useful discussion. This work was supported by the 973 Project of the Ministry of Science and Technology of China (Grants 2014CB921500 and 2016YFA0300701), the National Natural Science Foundation of China (Grant 11574378), and the Strategic Priority Research Program of the Chinese Academy of Sciences (Grant XDB07030300). J.A.A. is grateful for the financial support of Spanish MINECO Project MAT2013-41099-R. The work at ORNL HFIR (H.C. and C.d.C.) was sponsored by the Scientific User Facilities Division, Office of Science, Basic Energy Sciences, U.S. Department of Energy.

REFERENCES

(1) Long, Y. W.; Hayashi, N.; Saito, T.; Azuma, M.; Muranaka, S.; Shimakawa, Y. Temperature-induced A−B intersite charge transfer in an A-site-ordered $LaCu_3Fe_4O_{12}$ perovskite. *Nature* **2009**, *458*, 60−64.

(2) Zeng, Z.; Greenblatt, M.; Subramanian, M. A.; Croft, M. Large Low-Field Magnetoresistance in Perovskite-type $CaCu_3Mn_4O_{12}$ without Double Exchange. *Phys. Rev. Lett.* **1999**, *82*, 3164−3167.

DOI: 10.1021/acs.chemmater.6b03785
Chem. Mater. 2016, 28, 8988−8996

(3) Ramirez, A. P.; Subramanian, M. A.; Gardel, M.; Blumberg, G.; Li, D.; Vogt, T.; Shapiro, S. M. Giant Dielectric Constant Response in a Copper-Titanate. *Solid State Commun.* **2000**, *115*, 217−220.
(4) Homes, C. C.; Vogt, T.; Shapiro, S. M.; Wakimoto, S.; Ramirez, A. P. Optical Response of High-Dielectric-Constant Perovskite-Related Oxide. *Science* **2001**, *293*, 673−676.
(5) Alonso, J. A.; Sánchez-Benítez, J.; De Andrés, A.; Martínez-Lope, M. J.; Casais, M. T.; Martínez, J. L. Enhanced Magnetoresistance in the Complex Perovskite $LaCu_3Mn_4O_{12}$. *Appl. Phys. Lett.* **2003**, *83*, 2623−2625.
(6) Takata, K.; Yamada, I.; Azuma, M.; Takano, M.; Shimakawa, Y. Magnetoresistance and Electronic Structure of the Half-Metallic Ferrimagnet $BiCu_3Mn_4O_{12}$. *Phys. Rev. B: Condens. Matter Mater. Phys.* **2007**, *76*, 024429.
(7) Yamada, I.; Takata, K.; Hayashi, N.; Shinohara, S.; Azuma, M.; Mori, S.; Muranaka, S.; Shimakawa, Y.; Takano, M. A Perovskite Containing Quadrivalent Iron as a Charge-Disproportionated Ferrimagnet. *Angew. Chem., Int. Ed.* **2008**, *47*, 7032−7035.
(8) Long, Y. W.; Saito, T.; Tohyama, T.; Oka, K.; Azuma, M.; Shimakawa, Y. Intermetallic Charge Transfer in A-Site-Ordered Double Perovskite $BiCu_3Fe_4O_{12}$. *Inorg. Chem.* **2009**, *48*, 8489−8492.
(9) Mezzadri, F.; Calestani, G.; Calicchio, M.; Gilioli, E.; Bolzoni, F.; Cabassi, R.; Marezio, M.; Migliori, A. Synthesis and Characterization of Multiferroic $BiMn_7O_{12}$. *Phys. Rev. B: Condens. Matter Mater. Phys.* **2009**, *79*, 100106.
(10) Long, Y. W.; Shimakawa, Y. Intermetallic Charge Transfer between A-site Cu and B-site Fe in A-site-ordered Double Perovskites. *New J. Phys.* **2010**, *12*, 063029.
(11) Yamada, I.; Tsuchida, K.; Ohgushi, K.; Hayashi, N.; Kim, J.; Tsuji, N.; Takahashi, R.; Matsushita, M.; Nishiyama, N.; Inoue, T.; Irifune, T.; Kato, K.; Takata, M.; Takano, M. Giant Negative Thermal Expansion in the Iron Perovskite $SrCu_3Fe_4O_{12}$. *Angew. Chem., Int. Ed.* **2011**, *50*, 6579−6582.
(12) Zhang, G. Q.; Dong, S.; Yan, Z. B.; Guo, Y. Y.; Zhang, Q. F.; Yunoki, S.; Dagotto, E.; Liu, J. M. Multiferroic properties of $CaMn_7O_{12}$. *Phys. Rev. B: Condens. Matter Mater. Phys.* **2011**, *84*, 174413.
(13) Long, Y. W.; Kawakami, T.; Chen, W. T.; Saito, T.; Watanuki, T.; Nakakura, Y.; Liu, Q. Q.; Jin, C. Q.; Shimakawa, Y. Pressure Effect on Intersite Charge Transfer in A-site-Ordered Double-Perovskite-Structure Oxide. *Chem. Mater.* **2012**, *24*, 2235−2239.
(14) Wang, X.; Chai, Y. S.; Zhou, L.; Cao, H. B.; Cruz, C. D.; Yang, J. Y.; Dai, J. H.; Yin, Y. Y.; Yuan, Z.; Zhang, S. J.; Yu, R. Z.; Azuma, M.; Shimakawa, Y.; Zhang, H. M.; Dong, S.; Sun, Y.; Jin, C. Q.; Long, Y. W. Observation of Magnetoelectric Multiferroicity in a Cubic Perovskite System: $LaMn_3Cr_4O_{12}$. *Phys. Rev. Lett.* **2015**, *115*, 087601.
(15) Prodi, A.; Gilioli, E.; Gauzzi, A.; Licci, F.; Marezio, M.; Bolzoni, F.; Huang, Q.; Santoro, A.; Lynn, J. W. Charge, Orbital and Spin Ordering Phenomena in the Mixed Valence Manganite $(NaMn^{3+}_3)(Mn^{3+}_2Mn^{4+}_2)O_{12}$. *Nat. Mater.* **2004**, *3*, 48−52.
(16) Long, Y. W.; Saito, T.; Mizumaki, M.; Agui, A.; Shimakawa, Y. Various Valence States of Square-Coordinated Mn in A-Site-Ordered Perovskites. *J. Am. Chem. Soc.* **2009**, *131*, 16244−16247.
(17) Prodi, A.; Gilioli, E.; Cabassi, R.; Bolzoni, F.; Licci, F.; Huang, Q. Z.; Lynn, J. W.; Affronte, M.; Gauzzi, A.; Marezio, M. Magnetic structure of the high-density single-valent e_g Jahn-Teller system $LaMn_7O_{12}$. *Phys. Rev. B: Condens. Matter Mater. Phys.* **2009**, *79*, 085105.
(18) Senn, M. S.; Chen, W. T.; Saito, T.; García-Martín, S.; Attfield, J. P.; Shimakawa, Y. B-Cation Order Control of Magnetism in the 1322 Perovskite $CaCu_3Fe_2Nb_2O_{12}$. *Chem. Mater.* **2014**, *26*, 4832−4837.
(19) Goodenough, J. B. Theory of the Role of Covalence in the Perovskite-Type Manganites [La, *M*(II)] MnO_3. *Phys. Rev.* **1955**, *100*, 564−573.
(20) Kanamori, J. Superexchange Interaction and Symmetry Properties of Electron Orbitals. *J. Phys. Chem. Solids* **1959**, *10*, 87−98.
(21) Azuma, M.; Takata, K.; Saito, T.; Ishiwata, S.; Shimakawa, Y.; Takano, M. Designed Ferromagnetic, Ferroelectric Bi_2NiMnO_6. *J. Am. Chem. Soc.* **2005**, *127*, 8889−8892.
(22) Yi, W.; Princep, A. J.; Guo, Y. F.; Johnson, R. D.; Khalyavin, D.; Manuel, P.; Senyshyn, A.; Presniakov, I. A.; Sobolev, A. V.; Matsushita, Y.; Tanaka, M.; Belik, A. A.; Boothroyd, A. T. Sc_2NiMnO_6: A Double-Perovskite with a Magnetodielectric Response Driven by Multiple Magnetic Orders. *Inorg. Chem.* **2015**, *54*, 8012−8021.
(23) Yi, W.; Liang, Q. F.; Matsushita, Y.; Tanaka, M.; Belik, A. A. High-Pressure Synthesis, Crystal Structure, and Properties of In_2NiMnO_6 with Antiferromagnetic Order and Field-Induced Phase Transition. *Inorg. Chem.* **2013**, *52*, 14108−14115.
(24) Asai, K.; Fujiyoshi, K.; Nishimori, N.; Satoh, Y.; Kobayashi, Y.; Mizoguchi, M. Magnetic Properties of $REMe_{0.5}Mn_{0.5}O_3$ (RE = Rare Earth Element, Me = Ni, Co). *J. Phys. Soc. Jpn.* **1998**, *67*, 4218−4228.
(25) Booth, R. J.; Fillman, R.; Whitaker, H.; Nag, A.; Tiwari, R. M.; Ramanujachary, K. V.; Gopalakrishnan, J.; Lofland, S. E. An Investigation of Structural, Magnetic and Dielectric Properties of R_2NiMnO_6 (R = rare earth, Y). *Mater. Res. Bull.* **2009**, *44*, 1559−1564.
(26) Manna, K.; Bera, A. K.; Jain, M.; Elizabeth, S.; Yusuf, S. M.; Anil Kumar, P. S. Structural-Modulation-Driven Spin Canting and Reentrant Glassy Magnetic Phase in Ferromagnetic Lu_2MnNiO_6. *Phys. Rev. B: Condens. Matter Mater. Phys.* **2015**, *91*, 224420.
(27) Retuerto, M.; Muñoz, Á.; Martínez-Lope, M. J.; Alonso, J. A.; Mompeán, F. J.; Fernández-Díaz, M. T.; Sánchez-Benítez, J. Magnetic Interactions in the Double Perovskites R_2NiMnO_6 (R = Tb, Ho, Er, Tm) Investigated by Neutron Diffraction. *Inorg. Chem.* **2015**, *54*, 10890−10900.
(28) Nhalil, H.; Nair, H. S.; Kumar, C. M. N.; Strydom, A. M.; Elizabeth, S. Ferromagnetism and the Effect of Free Charge Carriers on Electric Polarization in the Double Perovskite Y_2NiMnO_6. *Phys. Rev. B: Condens. Matter Mater. Phys.* **2015**, *92*, 214426.
(29) Sánchez-Benítez, J.; Martínez-Lope, M. J.; Alonso, J. A.; García-Muñoz, J. L. Magnetic and Structural Features of the $NdNi_{1-x}Mn_xO_3$ Perovskite Series Investigated by Neutron Diffraction. *J. Phys.: Condens. Matter* **2011**, *23*, 226001.
(30) Rogado, N. S.; Li, J.; Sleight, A. W.; Subramanian, M. A. Magnetocapacitance and Magnetoresiatance Near Room Temperature in a Ferromagnetic Semiconductor: La_2NiMnO_6. *Adv. Mater.* **2005**, *17*, 2225−2227.
(31) Rietveld, H. M. A Profile Refinement Method for Nuclear and Magnetic Structures. *J. Appl. Crystallogr.* **1969**, *2*, 65−71.
(32) Larson, A. C.; Von Dreele, R. B. Los Alamos National Laboratory Report LAUR; Los Alamos National Laboratory: Los Alamos, NM, 2000; pp 86−748.
(33) Rodríguez-Carvajal, J. Recent Advances in Magnetic Structure Determination by Neutron Powder Diffraction. *Phys. B* **1993**, *192*, 55−69.
(34) Singh, D. J.; Nordstrom, L. *Plane Waves, Pseudopotentials and the LAPW Method*, 2nd ed.; Springer: Berlin, 2006.
(35) Sjöstedt, E.; Nordström, L.; Singh, D. J. An Alternative Way of Linearizing the Augmented Plane-Wave Method. *Solid State Commun.* **2000**, *114*, 15−20.
(36) Blaha, P.; Schwarz, K.; Madsen, G. K. H.; Kvasnicka, D.; Luitz, J. *WIEN2K, An Augmented Plane Wave Plus Local Orbitals Program for Calculating Crystal Properties*; Technische Universitat Wien: Vienna, 2002.
(37) Laskowski, R.; Madsen, G. K. H.; Blaha, P.; Schwarz, K. Magnetic Structure and Electric-Field Gradients of Uranium Dioxide: An Ab Initio Study. *Phys. Rev. B: Condens. Matter Mater. Phys.* **2004**, *69*, 140408.
(38) Perdew, J. P.; Burke, K.; Ernzerhof, M. Generalized Gradient Approximation Made Simple. *Phys. Rev. Lett.* **1996**, *77*, 3865−3868.
(39) Anisimov, V. I.; Solovyev, I. V.; Korotin, M. A.; Czyzyk, M. T.; Sawatzky, G. A. Density-Functional Theory and NiO Photoemission Spectra. *Phys. Rev. B: Condens. Matter Mater. Phys.* **1993**, *48*, 16929−16934.
(40) Byeon, S. H.; Lufaso, M. W.; Parise, J. B.; Woodward, P. M.; Hansen, T. High-Pressure Synthesis and Characterization of Perovskites with Simultaneous Ordering of Both the A- and B-Site Cations, $CaCu_3Ga_2M_2O_{12}$ (M = Sb, Ta). *Chem. Mater.* **2003**, *15*, 3798−3804.

DOI: 10.1021/acs.chemmater.6b03785
Chem. Mater. 2016, 28, 8988−8996

(41) Chen, W. T.; Mizumaki, M.; Seki, H.; Senn, M. S.; Saito, T.; Kan, D.; Attfield, J. P.; Shimakawa, Y. A Half-Metallic A- and B-Site-Ordered Quadruple Perovskite Oxide $CaCu_3Fe_2Re_2O_{12}$ with Large Magnetization and a High Transition Temperature. *Nat. Commun.* **2014**, *5*, 3909.
(42) Brown, I. D.; Altermatt, D. Bond-Valence Parameters Obtained from a Systematic Analysis of the Inorganic Crystal Structure Database. *Acta Crystallogr., Sect. B: Struct. Sci.* **1985**, *41*, 244−247.
(43) Brese, N. E.; O'Keeffe, M. Bond-Valence Parameters for Solids. *Acta Crystallogr., Sect. B: Struct. Sci.* **1991**, *47*, 192−197.
(44) Inaguma, Y.; Tanaka, K.; Tsuchiya, T.; Mori, D.; Katsumata, T.; Ohba, T.; Hiraki, K.; Takahashi, T.; Saitoh, H. Synthesis, Structural Transformation, Thermal Stability, Valence State, and Magnetic and Electronic Properties of $PbNiO_3$ with Perovskite- and $LiNbO_3$-Type Structures. *J. Am. Chem. Soc.* **2011**, *133*, 16920−16929.
(45) Hu, Z.; Mazumdar, C.; Kaindl, G.; de Groot, F. M. F.; Warda, S. A.; Reinen, D. Valence Electron Distribution in $La_2Li_{1/2}Cu_{1/2}O_4$, $Nd_2Li_{1/2}Ni_{1/2}O_4$, and $La_2Li_{1/2}Co_{1/2}O_4$. *Chem. Phys. Lett.* **1998**, *297*, 321−328.
(46) Hu, Z.; Golden, M. S.; Fink, J.; Kaindl, G.; Warda, S. A.; Reinen, D.; Mahadevan, P.; Sarma, D. D. Hole Distribution between the Ni 3*d* and O 2*p* Orbitals in $Nd_{2-x}Sr_xNiO_{4-\delta}$. *Phys. Rev. B: Condens. Matter Mater. Phys.* **2000**, *61* (5), 3739−3744.
(47) Tohyama, T.; Saito, T.; Mizumaki, M.; Agui, A.; Shimakawa, Y. Antiferromagnetic Interaction between A′-Site Mn Spins in A-Site-Ordered Perovskite $YMn_3Al_4O_{12}$. *Inorg. Chem.* **2010**, *49*, 2492−2495.
(48) Kim, D. H.; Lee, E.; Kim, H. W.; Kolesnik, S.; Dabrowski, B.; Kang, C. J.; Kim, M.; Min, B. I.; Lee, H. K.; Kim, J. Y.; Kang, J. S. Correlation between Mn and Ru Valence States and Magnetic Phases in $SrMn_{1-x}Ru_xO_3$. *Phys. Rev. B: Condens. Matter Mater. Phys.* **2015**, *91*, 075113.
(49) Byeon, S. H.; Lee, S. S.; Parise, J. B.; Woodward, P. M.; Hur, N. H. New Ferrimagnetic Oxide $CaCu_3Cr_2Sb_2O_{12}$: High-Pressure Synthesis, Structure, and Magnetic Properties. *Chem. Mater.* **2005**, *17*, 3552−3557.
(50) Deng, H. S.; Liu, M.; Dai, J. H.; Hu, Z. W.; Kuo, C. Y.; Yin, Y. Y.; Yang, J. Y.; Wang, X.; Zhao, Q.; Xu, Y. J.; Fu, Z. M.; Cai, J. W.; Guo, H. Z.; Jin, K. J.; Pi, T. W.; Soo, Y. L.; Zhou, G. H.; Cheng, J. G.; Chen, K.; Ohresser, P.; Yang, Y. F.; Jin, C. Q.; Tjeng, L. H.; Long, Y. W. Strong Enhancement of Spin Ordering by A-site Magnetic Ions in the Ferrimagnet $CaCu_3Fe_2Os_2O_{12}$. *Phys. Rev. B* **2016**, *94*, 024414.
(51) Toyoda, M.; Saito, T.; Yamauchi, K.; Shimakawa, Y.; Oguchi, T. Superexchange Interaction in the A-site Ordered Perovskite $YMn_3Al_4O_{12}$. *Phys. Rev. B: Condens. Matter Mater. Phys.* **2015**, *92*, 014420.
(52) Morrow, R.; Mishra, R.; Restrepo, O. D.; Ball, M. R.; Windl, W.; Wurmehl, S.; Stockert, U.; Büchner, B.; Woodward, P. M. Independent Ordering of Two Interpenetrating Magnetic Sublattices in the Double Perovskite Sr_2CoOsO_6. *J. Am. Chem. Soc.* **2013**, *135*, 18824−18830.
(53) Lv, S. H.; Li, H. P.; Liu, X. J.; Meng, J. Mn-Cr Intersite Independent Magnetic Behavior and Electronic Structures of $LaMn_3Cr_4O_{12}$: Study from First-Principles. *J. Appl. Phys.* **2011**, *110*, 023711.
(54) Gardner, J. S.; Gingras, M. J. P.; Greedan, J. E. Magnetic pyrochlore oxides. *Rev. Mod. Phys.* **2010**, *82*, 53−107.

DOI: 10.1021/acs.chemmater.6b03785
Chem. Mater. 2016, 28, 8988−8996